Check for updates

Molybdenum sulfo-selenide nanocomposites with carbon nanotubes and reduced graphene oxide for photocatalytic hydrogen evolution reaction†

Namsheer K.,[a] K. Pramoda,*[a] Kothanahally S. Sharath Kumar,[b] Sithara Radhakrishnan[a] and Chandra Sekhar Rout [ID] *[a]

We report a facile method for the preparation of nanocomposites of molybdenum sulfo-selenide (MoS_xSe_{1-x}) with carbon nanotubes (CNTs) and reduced graphene oxide (RGO) *via* a solvothermal approach. The synthesized MoSSe@CNT and MoSSe@RGO nanocomposites are characterized by various microscopic and spectroscopic methods. We investigated the photocatalytic hydrogen evolution reaction (HER) performance of the MoSSe@CNT and MoSSe@RGO nanocomposites using eosin Y dye as a sensitizer, and triethanolamine as a sacrificial agent, under UV-vis light (Xenon lamp; 400 W) illumination. The highest photocatalytic HER activity of 5016 μmol h^{-1} g^{-1} is achieved with the MoSSe@RGO nanocomposite, which is ~3 times higher than that of the bare MoS_xSe_{1-x} nanostructure (1754 μmol h^{-1} g^{-1}). Meanwhile, the MoSSe@CNT nanocomposite shows a somewhat lower activity of 3622 μmol h^{-1} g^{-1}. These results indicate that the growth of MoSSe over conducting CNT/RGO improves the HER activity of the MoSSe nanostructure, but 2D RGO offers more facile electron-transfer routes compared to 1D CNTs. The HER activity of the nanocomposites is comparable with some of the recently reported 2D transition-metal-based nanocomposites reported in the literature. Photoluminescence studies indicate that the facile charge-transfer interaction between MoSSe and RGO/SWCNT is responsible for the remarkable HER activity of the nanocomposites. Additionally, more exposed edge sites of vertically grown discrete MoSSe nanostructures in the case of the nanocomposites, as suggested by microscopic studies, plausibly also contribute to the improved photocatalytic HER activity.

1. Introduction

The generation of hydrogen by photocatalytic, electrocatalytic, and photo-electrocatalytic approaches has gained significant attention in recent years due to the rise in demand for renewable hydrogen.[1–3] Plants transform solar energy into chemical energy with a quantum yield of near unity wherein two photosystems (photosystem I and photosystem II) concurrently absorb the light and in the cascade of electron-relay channels help the spatial separation of charges.[4,5] Numerous efforts have been made to mimic natural photosynthesis in the laboratory artificially, to produce hydrogen and oxygen by splitting water.[6–8] A viable strategy for direct solar-to-hydrogen conversion has been reported to be photocatalytic water splitting over semiconductor materials without utilizing any fossil fuel or emitting carbon dioxide.[9–11] Thermodynamically, water splitting is an uphill reaction, and it involves a large Gibb's free energy change of 237 kJ mol^{-1}. Hence, several researchers have tried to generate hydrogen and oxygen from water using semiconductor photocatalysts to make water splitting viable.[12–14] Photo-induced water splitting on TiO_2 electrodes was first reported by Fujishima and Honda in 1972.[15] Since then, several photosystems have been developed, which can imitate natural photosynthesis to generate hydrogen and oxygen from water by utilizing solar energy.[16–18] Photocatalysts utilized for water splitting range from narrow band gap to wide band gap materials.[19–21] Generally, narrow-band gap photosystems are preferred due to their comparatively higher visible-light absorption capacity. To achieve overall water splitting, the bottom of the CB of the semiconductor should be more negative than the H^+/H_2 reduction potential

[a] *Centre for Nano and Material Sciences, Jain (Deemed-to-be-University), Jain Global Campus, Kanakapura, Bangalore-562112, Karnataka, India. E-mail: k.pramoda@jainuniversity.ac.in, r.chandrasekhar@jainuniversity.ac.in*

[b] *DOS in Chemistry, Manasagangotri, University of Mysore, Mysuru-570006, India*

(-0.41 V *vs.* NHE) and the top of the VB must be more positive than the water oxidation potential ($+0.82$ V *vs.* NHE).[22,23]

Since the discovery of graphene with novel properties,[24,25] two-dimensional (2D) transition metal dichalcogenides (TMDCs) have gained more importance due to their wide range of applications ranging from electronics[26,27] to catalysis.[28,29] The library of 2D TMDCs, including MoS_2,[30] $MoSe_2$,[31] WS_2,[32] WSe_2,[33] and $MoTe_2$,[34] has been utilized in various photocatalytic/electro-catalytic applications due to their suitable physicochemical characteristics including large surface area, earth-abundant characteristics, and chemical inertness.[35] Normally, three processes are involved in photocatalytic water splitting: (1) light absorption by a catalyst, (2) charge-carrier generation/separation, and lastly (3) redox reactions at the catalyst's surface. The first criterion in the case of 2D materials is realized by tuning the bandgap either by phase engineering,[36] alloying,[37] defect engineering,[38] or heterostructuring,[39] while the thinning of the number of layers makes shorter travel distances for charge carriers to reach the surface active sites.[22,23] Finally, the third condition can be fulfilled by a high surface area of 2D materials, which offers a significant number of catalytically active sites.[40] On the other hand, bulk counterpart utilization is constrained in photocatalytic water splitting due to their poor light absorption, high charge-carrier recombination rate, and dearth of catalytically active sites.

Among the 2D TMDCs, MoS_2 is being extensively utilized as a catalyst for photocatalytic/electrocatalytic water reduction reactions under acidic as well as alkaline conditions because of the favourably located conduction band minimum (CBM), which is more negative than the water reduction potential (H^+/H_2 0 V *vs.* NHE) for feasible HER.[41] Structurally, individual MoS_2 layers consist of Mo metal atomic planes sandwiched between S atomic planes. Each monolayer is held together by weak van der Waals forces, forming a stacked structure.[42,43] The electrical and optical properties of MoS_2 can be tuned with a number of layers.[43] MoS_2 maintains various polymorphic forms, tetragonal (1T) and hexagonal (2H), depending on the procedure adopted for its synthesis. $1T-MoS_2$ possesses a tetragonal crystal structure with octahedral (O_h) coordination of the metal and chalcogen atoms while $2H-MoS_2$ shows a hexagonal symmetry with trigonal prismatic (D_{3H}) coordination. On Li-intercalation, $2H-MoS_2$ is converted to a less stable 1T-phase.[23,44] The 1T-phase is reported to be metallic, while $2H-MoS_2$ displays semiconductor characteristics. Due to their similar electronic configuration to Pt, theoretical models and experimental findings reveal that $2H-MoS_2$ has tremendous potential for energy conversion applications.[45] However, the semiconducting characteristics and other stability issues associated with $2H-MoS_2$ (hexagonal phase), which is the most stable form at room temperature, limit the application of MoS_2 as an HER catalyst.[46] Theoretical investigations revealed that the edge sites of $2H-MoS_2$ are the only active sites for the water reduction reaction while the basal plane remains inert.[47] Combining $2D-MoS_2$ with electrically conducting carbon nanotubes (CNTs) or graphene is reported to enhance the HER characteristics of bare TMDCs.[48] The growth of 2D TMDCs on electrically conducting CNTs or graphene possibly reduces charge-transfer resistance and also increases the interaction between the electrolyte and the active sites of MoS_2, since CNTs or graphene act as the template for the uniform growth of TMDCs.

Forming a solid-solution of MoS_2 with $MoSe_2$ is another interesting approach to enhance the MoS_2 HER activity as these solid-solutions show better charge-transfer characteristics, compared to individual components due to partial conversion of the semiconducting hexagonal 2H-phase to the metallic tetragonal 1T-phase.[49] Secondly, making solid solutions imports more active edge sites due to the formation of discrete MoS(Se) domains and also enhances dispersibility, thereby giving higher H_2 yield. Some of these MoS_xSe_{1-x} displayed stable hydrogen evolution under electrolytic conditions over a wide pH range.[50] However, a very limited number of studies focused on photocatalytic HER applications of these MoS_xSe_{1-x} solid solutions.[51] In addition, MoS_xSe_{1-x} solid-solution nanocomposites with CNTs or graphene are not reported for photocatalytic HER applications. Among various carbon supports, CNTs and graphene are considered good support materials because of their high electronic conductivity, large surface area, and ease of achieving surface modification, which helps to anchor active components.[52,53]

In the present study, bare MoS_xSe_{1-x} nanoflowers are synthesized by reacting ammonium molybdate tetrahydrate, thiourea, and selenium powder *via* a hydrothermal approach. Furthermore, the addition of carboxyl-functionalized multi-walled carbon nanotubes (MWCNTs) and graphene oxide (GO) independently during MoS_xSe_{1-x} nanoflower formation results in the growth of MoS_xSe_{1-x} over the CNT or graphene surface. The dye-sensitized water reduction activity of the synthesized nanocomposites is investigated. We find the highest H_2 evolution rate of 5016 µmol h^{-1} g^{-1} with the MoSSe@RGO heterostructure, whereas the MoSSe@CNT hybrid shows somewhat lower HER activity of 3622 µmol h^{-1} g^{-1}.

2. Results and discussion

Fig. 1 shows the schematic of the synthesis procedure employed to prepare the MoSSe@CNT and MoSSe@RGO heterostructures *via* the hydrothermal method. Initially, thiourea and selenium precursors (with hydrazine hydrate) decompose at high-temperature to give S^{2-} and Se^{2-} species, respectively, *via* hydrolyzation reaction as described in eqn (1)–(3). On the other hand, the ammonium molybdate precursor under reducing conditions and at high-temperature yields MoO_3 (eqn (4)).

Subsequently, the anion exchange reaction between MoO_3 and S^{2-}/Se^{2-} species yields a MoS_xSe_{1-x} intermediate. Finally, MoS_xSe_{1-x} is reduced to 1T and 2H-phases as the final product (eqn (5)).[54] The microstructure and surface morphology of the synthesized MoSSe@CNT and MoSSe@RGO nanocomposites are investigated using a field emission scanning electron microscope (FESEM). Bare MoSSe exhibits a flower-shaped morphology with vertically oriented petals on the spherical surface, as shown in Fig. (2a and d). After the addition of

$$NH_2CSNH_2 + 2H_2O \rightarrow H_2S + 2NH_3 + CO_2 \quad (1)$$

$$H_2S + 2OH^- \rightarrow 2H_2O + S^{2-} \quad (2)$$

$$Se + (NH_2)_2\,H_2O \rightarrow Se^{2-} + \text{by-product} \quad (3)$$

$$(NH_4)_6Mo_7O_{24} \cdot 4H_2O \rightarrow 7\,MoO_3 + 7H_2O + 6NH_3 \quad (4)$$

$$7\,MoO_3 + S^{2-} + Se^{2-} \rightarrow (\,MoS_xSe_{1-x}\,)_{\text{Intermediate}}$$
$$\rightarrow MoS_xSe_{1-x}\ (1T/2H) \quad (5)$$

Fig. 1 A schematic illustration demonstrating the synthesis of bare MoSSe, MoSSe@CNT, and MoSSe@RGO nanocomposites *via* a solvothermal approach and the right panel showing the various reaction intermediates generated during MoSSe growth.

RGO/CNT, MoSSe petals predominantly grown on 1D-CNT/2D-RGO are evident in the FESEM images shown in Fig. 2(b and e) and (c and f), which suggests that the functional groups of CNT/RGO act as templates for MoSSe growth. Initially, positively charged molybdenum precursors get adsorbed onto the carboxyl-functionalized MWCNTs or RGO (negative zeta potential) surface by electrostatic interaction. Later, the reaction between molybdenum and sulfur/selenium precursors under hydrothermal conditions yields uniformly grown MoSSe over CNTs or RGO. Fig. S1 (ESI†) shows the zeta potential plots for the functionalized SWCNTs, RGO, MoSSe@CNT, and MoSSe@RGO composites. The functionalized SWCNTs and RGO show negative zeta potential of −34 and −32 mV, respectively, due to the surface –OH and carboxyl groups. In the case of the MoSSe@CNT (−8 mV) and MoSSe@RGO (−4 mV) nanocomposites, the zeta potential shifted to a neutral value possibly due to electrostatic adsorption of MoSSe precursors on RGO/CNT and later elimination of functionalities due to reducing conditions under hydrothermal conditions. Thus, zeta potential studies indicate that the surface functional groups of SWCNT/RGO act as templates for the growth of MoSSe nanoflowers.

The defect-rich CNT/RGO templates perhaps minimize restacking/agglomeration of MoSSe petals and result in the growth of isolated MoSSe sheets over the CNT/RGO matrix. Formation of the hybrid structure provides enhanced active surface area and edge sites, leading to higher photocatalytic activity as compared to the bare MoSSe nanostructures. Besides, the underlying electrically conducting CNT/RGO matrix improves the overall charge-transfer efficiency, and thereby the composites are expected to display higher photocatalytic activity. For comparison purposes, FESEM images of the carboxyl-functionalized MWCNTs and graphene oxide are shown in Fig. S2a and b (ESI†), respectively.

Fig. 3 shows transmission electron microscope (TEM) and high resolution TEM (HRTEM) images of the bare MoSSe, MoSSe@CNT and MoSSe@RGO nanocomposites. The HRTEM images of MoSSe@RGO and MoSSe@CNT shown in Fig. 3b and d, respectively, revealed the direct growth of MoSSe over the functionalized CNT/RGO surface. These results indicate that the surface functional groups of CNT/RGO act as anchor sites for nucleation and growth of MoSSe nanostructures.

The powder X-ray diffraction pattern (PXRD) of the synthesized nanocomposites is recorded to investigate the phase
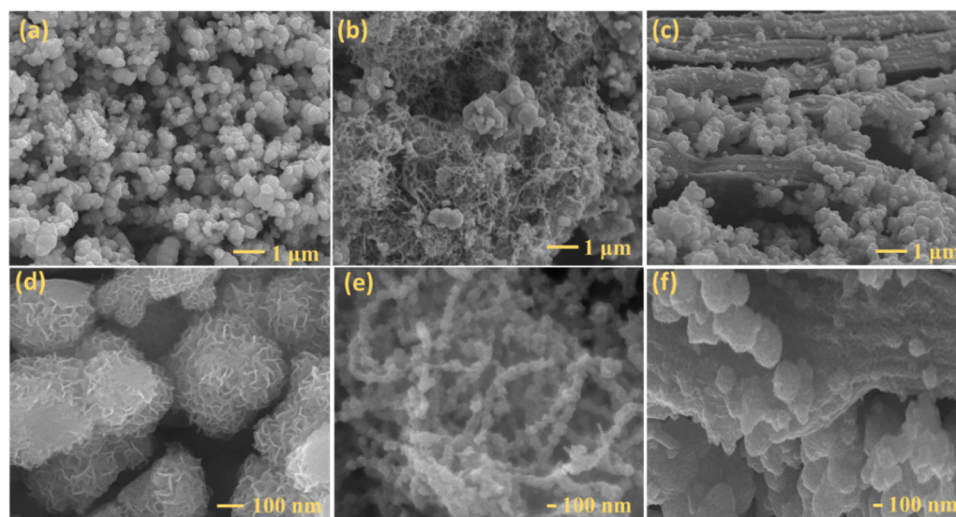

Fig. 2 Low and high-resolution FESEM images of (a) and (d) bare MoSSe, (b) and (e) MoSSe@CNT, and (c) and (f) MoSSe@RGO heterostructures.

Fig. 3 Low and high-resolution TEM images of (a) and (b) MoSSe@RGO (inset shows TEM image of bare MoSSe), and (c) and (d) MoSSe@CNT heterostructures.

purity and other structural aspects. Fig. 4(a) shows the PXRD pattern of the MoSSe nanoflowers, MoSSe@CNT, and MoSSe@RGO respectively. Bare MoSSe nanoflowers show diffraction peaks at 2θ of $9.2°$, $33.6°$, $43.6°$, and $56.6°$ attributed to (002), (100), (103), and (111) crystal planes, respectively, consistent with the JCPDS No: 37-1492 corresponding to 2H-MoS$_2$ nanosheets.[55] As per the literature, 1T/2H mixed phase MoS$_2$ shows the (002) plane of 1T and 2H-phases at 9.0 and 14.0°, respectively (JCPDS No. 37-1492). Bare MoSSe shows the main peak at 2θ of 9.0°, corresponding to the (002) plane of 1T-phase. While the peak at 14.0° attributed to the 2H-phase of the (002) plane is absent possibly due to the existence of a relatively higher proportion of the 1T-phase. However, the presence of

broad peaks at 33.6° and 43.6° indicates the presence of (110) and (103) planes of the 2H-phase,[56] indicating that the synthesized MoSSe is a mixture of 1T/2H-phase. In the case of the MoSSe@CNT and MoSSe@RGO nanocomposites, all the peaks corresponding to MoSSe are present along with a new peak at 25.6° corresponding to an inter-layer spacing of 0.35 nm between the stacked CNT/RGO evident, suggesting the growth of MoSSe over the CNT/RGO matrix.

Besides, we investigated the MoSSe@CNT and MoSSe@RGO nanocomposites by Raman spectroscopy to evaluate the MoSSe phase composition as well as the homogeneity of the nanocomposite (Fig. 4b) spectra.[57,58] Raman spectra recorded at various locations of the nanocomposite show peaks corresponding to both MoSSe and RGO/CNT, which confirms the homogeneity of the synthesized hybrids. The Raman spectra of the bare MoSSe display characteristic signals at 236, 283, and 336 cm^{-1}, which are attributed to J$_2$, E$_{1g}$, and J$_3$ phonon modes of the 1T-phase. This result is in agreement with the report of Gupta *et al.*[59] Meanwhile, the peak at 377 cm^{-1} corresponds to the E$_{2g}^1$ band of the 2H phase as reported by Jenjati *et al.*[60] In the case of the MoSSe@CNT and MoSSe@RGO heterostructure, the Raman peaks of the 1T/2H-phase are slightly redshifted as compared to bare MoSSe, which suggests the charge-transfer interaction between the hetero-components. Meanwhile, the 1343.5 and 1575 cm^{-1} peaks corresponding to the G and D bands of RGO, sp^3 and sp^2 hybridized carbon atoms, are also evident in the Raman spectra. X-ray photoelectron spectroscopy (XPS) is used to examine the phase purity and elemental composition of the MoSSe@RGO nanocomposite. The survey spectrum of the MoSSe@RGO nanocomposite shown in Fig. S3 (ESI†) displays the presence of only Mo, S, Se, and C elements, indicating that the nanocomposite synthesized is in a pure form and it is free from other impurities due to the starting precursors. The deconvoluted Mo 3d spectrum shows peaks at binding energies of 228.2 and 231.0 eV, which are attributed to the Mo^{4+} 3d$_{5/2}$ and Mo^{4+} 3d$_{3/2}$ components of MoSSe[60,61] (Fig. 5a). The other signals at 234.8 and 233.3 eV in the
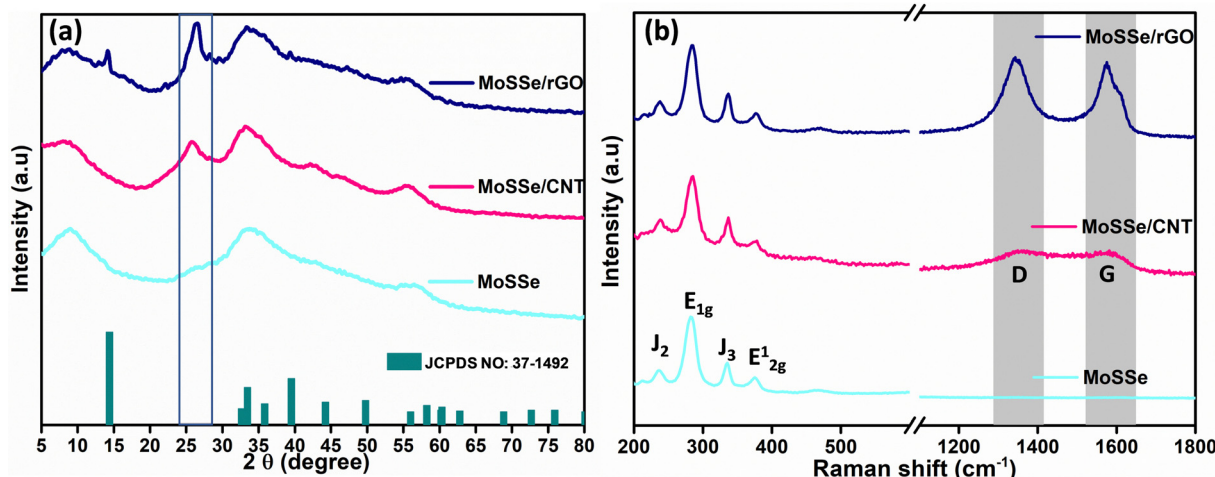

Fig. 4 (a) PXRD pattern and (b) Raman spectra of the bare MoSSe, MoSSe@CNT and MoSSe@RGO heterostructure.

Fig. 5 High-resolution X-ray photoelectron spectra of (a) Mo 3d, (b) S 2p, (c) Se 3d and (d) C 1s elements of the MoSSe@RGO nanocomposite.

MoSSe@RGO nanocomposite are likely ascribed to the presence of a small portion of Mo^{6+}.[62] The deconvoluted S 2p spectrum shows peaks at 161.1 and 162.5 eV corresponding to the S^{2-} $2p_{3/2}$ and S^{2-} $2p_{1/2}$ state (Fig. 5b) respectively.[63,64] Similarly, the Se 3d spectrum of the MoSSe@RGO nanocomposite (Fig. 5c), displays two peaks at 53.7 and 54.7 eV corresponding to Se^{2-} $3d_{5/2}$ and Se^{2-} $3d_{3/2}$, respectively.[65] Furthermore, the C 1s spectra are deconvoluted into three peaks. The peak at 284.6 eV corresponds to the graphitic carbon[66] and the peak at a binding energy of 286.0 eV is ascribed to hydroxyl groups and finally, the peak at 287.6 eV is attributed to the occurrence of a carbonyl group. The intensities corresponding to the oxygen functional groups, C–O and C=O, were negligible, suggesting the partial restoration of the sp^2 domains (Fig. 5d).[67] The XPS analysis confirms the presence of Mo, S, Se, and the reduced graphene matrix and the existence of a small proportion of Mo(VI) ions due to the presence of MoO_3 by the incomplete reduction of MoO_4^{2-} during the reaction conditions.

The photochemical HER activity of the MoSSe@CNT and MoSSe@RGO nanocomposite is investigated using eosin Y dye as a photosensitizer and tri ethanol amine as a sacrificial agent under UV-light illumination. The yields of H_2 evolved using the MoSSe@CNT and MoSSe@RGO nanocomposites along with the starting materials MoSSe, CNT, and RGO are shown in

Fig. 6(a and b). Pristine MoSSe shows HER activity of 1754 $\mu mol\ h^{-1}\ g^{-1}$ while the pristine SWCNTs and RGO display activity of 630 and 651 $\mu mol\ h^{-1}\ g^{-1}$, respectively. In contrast, the MoSSe@CNT and MoSSe@RGO nanocomposites exhibit the activity of 3622 and 5016 $\mu mol\ h^{-1}\ g^{-1}$, respectively. MoSSe@CNT shows a 2* times enhancement in HER activity compared to the pristine MoSSe while MoSSe@RGO shows a slightly higher enhancement in activity of 3* times. These results suggest that the growth of MoSSe nanostructures on the conducting CNT/RGO matrix enhances the HER activity. The functional groups of the underlying CNT or graphene networks act as nucleation sites for discrete MoSSe growth, which results in improved surface area and more exposed edge sites; thereby, the nanocomposites show higher HER activity.

The cycling stability tests revealed that MoSSe@RGO showed stable H_2 evolution throughout 30 h and 6 cycles, indicating the robust nature of the nanocomposites (Fig. 6c). Furthermore, structural changes in the MoSSe@RGO nanocomposites after the cyclic stability test were investigated using Raman spectra. It can be seen that there were no noticeable changes in the Raman spectra even after the 30 h cycling stability test, as shown in Fig. S4 (ESI†). The apparent quantum yield (AQY) measured on the optimum MoSSe/RGO catalyst at 420, 500, 600 and 700 nm is included in Fig. 6d. The AQY for
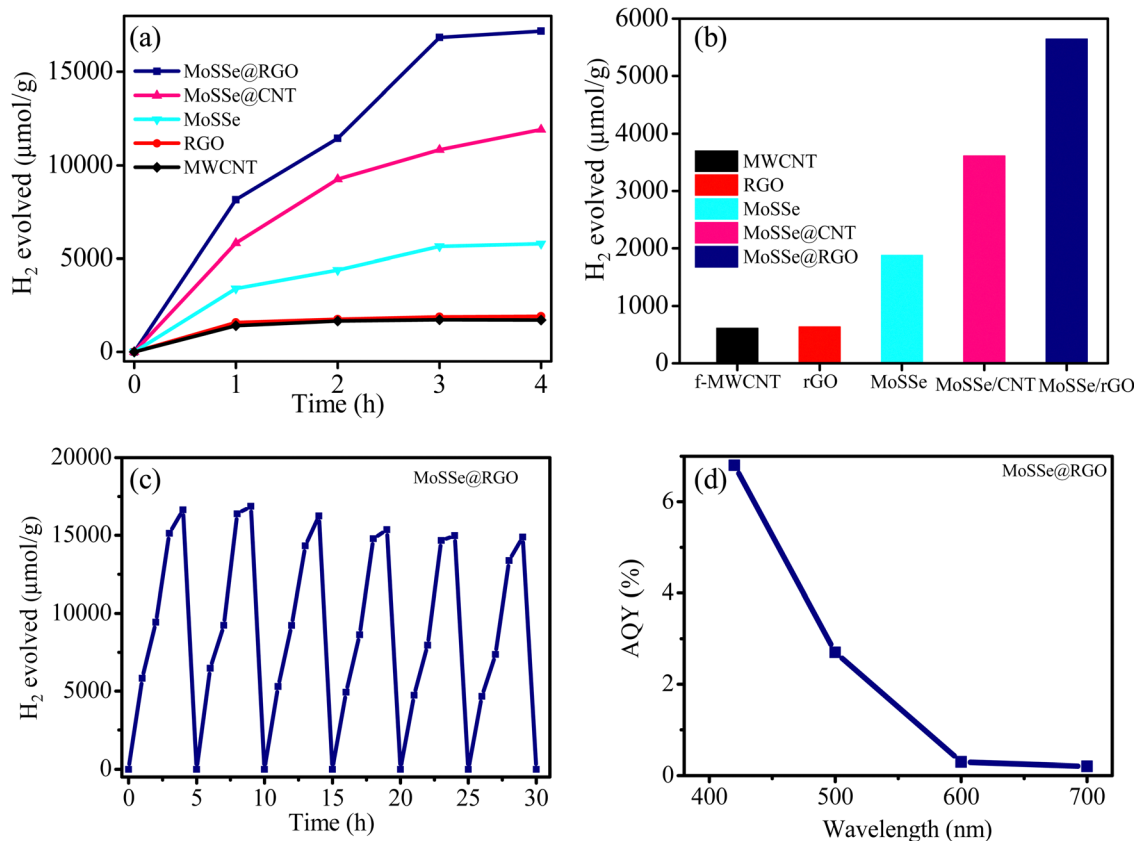
Fig. 6 (a) Photocatalytic H_2 evolution data of the bare MWCNTs, RGO, MoSSe, MoSSe@CNT, and MoSSe@RGO nanocomposites; (b) bar diagram showing the comparison of the HER activities of the samples; (c) cycling stability curve for MoSSe@RGO nanocomposites and (d) AQY measured on the optimum MoSSe/RGO catalyst at 420, 500, 600 and 700 nm.

the MoSSe/RGO catalyst is found to be 6.8% at 420 nm and 2.7% at 500 nm and it also exhibits some activity at 600 and 700 nm. In Table S1 (ESI†), we have compared the activity of the MoSSe@CNT and MoSSe@RGO nanocomposites with some of the other TMDC-based nanocomposites reported in the literature. The activity of the MoSSe@RGO nanocomposites is found to be comparable with some of the best reported TMDC-based systems.

The band gap of the bare MoSSe and MoSSe@RGO is obtained from a Tauc plot derived from the UV-vis spectra (Fig. 7a). The Tauc plot is obtained by plotting $h\nu$ *vs.* $(\alpha h\nu)^2$, where α is the absorption coefficient, h is the Planck constant and ν is the frequency of light. The obtained band gap energy value for the bare MoSSe and MoSSe@RGO nanocomposite is 2.2 and 1.8 eV, respectively. The band gap value of 1.8 eV obtained with MoSSe@RGO indicates that the composite is suitable for photocatalysis application in visible-light radiation. To investigate the band positions, XPS valence band spectra (Fig. 7b) and Mott–Schottky plots (Fig. 7c) were explored. The valence band (VB) XPS spectra of MoSSe@RGO revealed that the VB maximum of the MoSSe@RGO nanocomposite is at 1.19 eV. Furthermore, the corresponding conduction band (CB) minimum was obtained using the following equation:

$$E_{CB} = E_{VB} + E_g$$

where E_{CB} and E_{VB} correspond to CB potential and VB potential, respectively, and E_g is the band gap. Therefore, E_{CB} of

MoSSe@RGO is calculated to be at −0.61 eV. Photoluminescence spectra (PL) of eosin Y dye are also examined in the presence of the MoSSe@CNT and MoSSe@RGO nanocomposites since the HER of all of the above mentioned samples is carried out in the presence of photosensitizer eosin Y dye. Bare eosin Y shows an emission peak at 570 nm in aqueous conditions when the excitation wavelength is set at 490 nm, consistent with the previous literature reports.[68–70] As shown in Fig. 7(d), the emission band of EY at 570 nm is quenched with the addition of the nanocomposites, suggesting the transfer of an electron from photoexcited eosin Y (EY*) to the nanocomposites, which could possibly be utilized for the HER at the MoSSe active sites. Based on the above studies, we have proposed a schematic for the mechanism of the HER on the MoSSe@CNT and MoSSe@RGO nanocomposites in the presence of Eosin Y dye (Fig. 8). On photoexcitation, EY undergoes a series of transformations to give EY^{3*} and then EY^{-1}. The electron-rich EY$^-$ later transfers electrons to the active sites of MoSSe@CNT, namely the edge sites of MoSSe *via* sp^2 bonded CNT/graphene networks, where water reduction takes place. Furthermore, a relatively lower magnitude of MoSSe nanoflowers in the case of MoSSe@CNT and MoSSe@RGO compared to bare MoSSe as evidenced by the FESEM images specifies that more edge sites are accessible in the nanocomposites, thereby showing higher activity. To further support the
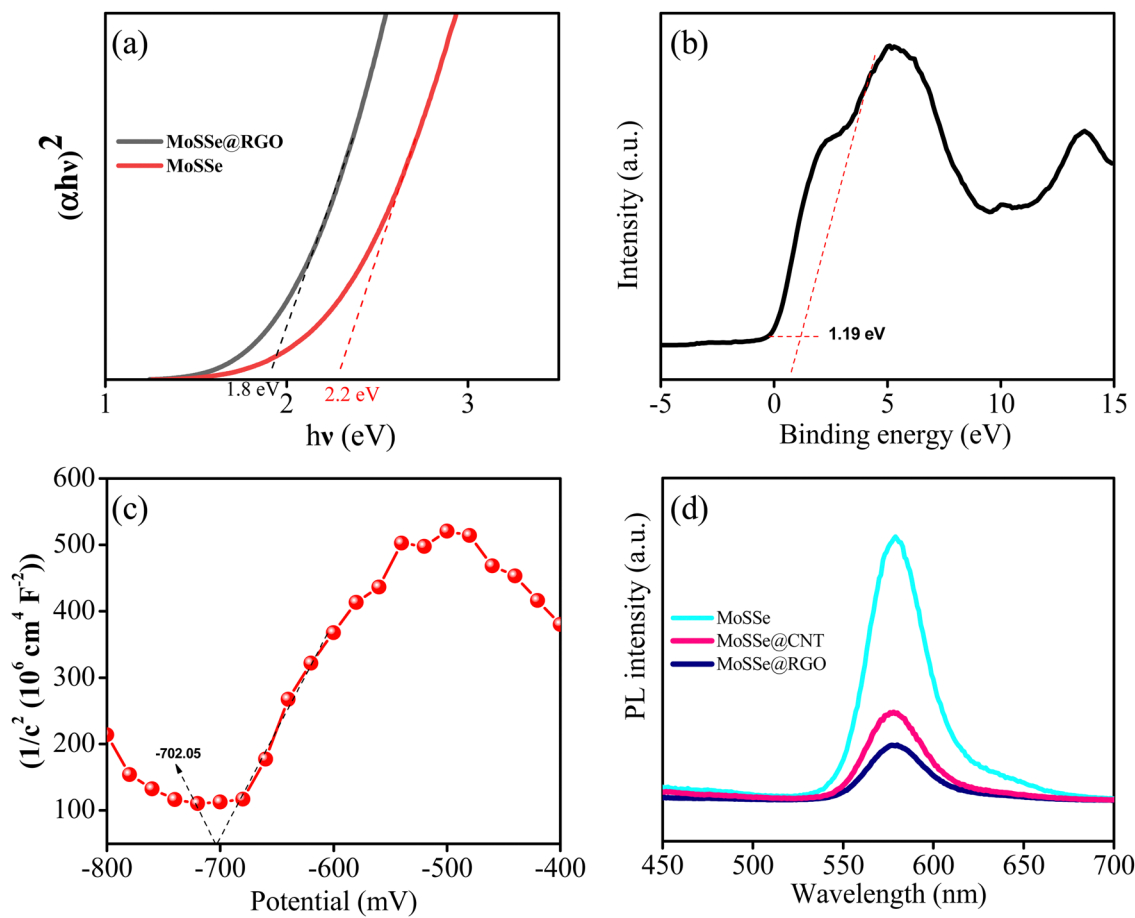
Fig. 7 (a) Tauc plot of MoSSe and the MoSSe@RGO nanocomposite; (b) VB XPS spectra and (c) Mott–Schottky plots of the MoSSe@RGO nanocomposite; (d) PL spectra of an aqueous solution of eosin Y (1.0×10^{-7} M, excitation wavelength = 490 nm) in the presence of MoSSe@CNT and MoSSe@RGO.

Fig. 8 (a) and (b) A schematic illustration representing the dye-sensitized photocatalytic HER mechanism of the MoSSe@RGO nanocomposites using TEOA sacrificial agent under visible-light irradiation. VBM (valence band minimum); CBM (conduction band maximum); HOMO (highest occupied molecular orbital); LUMO (lowest unoccupied molecular orbital).

elucidated mechanism, secondly, slightly higher enhancement in the case of MoSSe@RGO compared to MoSSe/SWCNT suggests that graphene provides a more efficient pathway for electron transfer due to its 2D nature.

3. Conclusions

In conclusion, we have successfully synthesized MoSSe@CNT and MoSSe@RGO nanocomposites by a facile hydrothermal method. Zeta potential studies indicate that the functionalized CNT/RGO matrix acts as a template for the growth of MoSSe nanostructures. The synthesized composites are examined for the photocatalytic hydrogen evolution reaction using eosin Y as a photosensitizer and triethanolamine as a sacrificial agent, under UV-vis light. Both the nanocomposites show satisfactory activity towards H_2 evolution, the activities being 3622 and 5016 μmol h^{-1} g^{-1} in the case of the MoSSe@CNT and MoSSe@RGO heterostructures, respectively. The HER activity of the nanocomposite is comparable with some of the 2D transition metal chalcogenide nanocomposites reported in the literature. The high HER activity of the MoSSe@CNT and MoSSe@RGO heterostructures as compared to bare MoSSe is attributed to the improved charge-transfer rate between the individual components and more exposed edge sites of MoSSe.

Author contributions

Namsheer K: performing experiment, data interpretation, and writing the original draft. Dr K. Pramoda: performing experiments, conceptualization, editing the draft, funding acquisition, and supervision. K. S. Sharath Kumar: performing some portions of the experimental part. Prof. Chandra Sekhar Rout: conceptualization, project administration, funding acquisition, supervision.

Conflicts of interest

The authors declare no conflict of interest.

Acknowledgements

References

1 S. Ghasemian, A. Faridzad, P. Abbaszadeh, A. Taklif, A. Ghasemi and R. Hafezi, An overview of global energy scenarios by 2040: identifying the driving forces using cross-impact analysis method, *Int. J. Environ. Sci. Technol.*, 2020, DOI: 10.1007/s13762-020-02738-5.

2 I. Staffell, D. Scamman, A. V. Abad, P. Balcombe, P. E. Dodds and P. Ekins, *et al.*, The role of hydrogen and fuel cells in the global energy system, *Energy Environ. Sci.*, 2019, **12**, 463–491, DOI: 10.1039/C8EE01157E.

3 J. W. Sheffield and Ç. Sheffield, *Assessment of Hydrogen Energy for Sustainable Development*, Springer, Netherlands, Dordrecht, 2007, DOI: 10.1007/978-1-4020-6442-5.

4 Y. Tachibana, L. Vayssieres and J. R. Durrant, Artificial photosynthesis for solar water-splitting, *Nat. Photonics*, 2012, **6**, 511–518, DOI: 10.1038/nphoton.2012.175.

5 Z. Han and R. Eisenberg, Fuel from Water: The Photochemical Generation of Hydrogen from Water, *Acc. Chem. Res.*, 2014, **47**, 2537–2544, DOI: 10.1021/ar5001605.

6 Z. Liang, J. Bai, L. Hao, R. Shen, P. Zhang and X. Li, Photodeposition of NiS Cocatalysts on g-C_3N_4 with Edge Grafting of 4-(1H-Imidazol-2-yl) Benzoic Acid for Highly Elevated Photocatalytic H_2 Evolution, *Adv. Sustainable Systems*, 2023, **7**, 2200143, DOI: 10.1002/adsu.202200143.

7 X. Wang, Y. Li, T. Li and Z. Jin, Synergistic Effect of Bimetallic Sulfide Enhances the Performance of CdS Photocatalytic Hydrogen Evolution, *Adv. Sustainable Systems*, 2023, **7**, 2200139, DOI: 10.1002/adsu.202200139.

8 M. Li, L. Zhang, X. Fan, M. Wu, Y. Du and M. Wang, *et al.*, Dual synergetic effects in MoS_2/pyridine-modified g-C_3N_4 composite for highly active and stable photocatalytic hydrogen evolution under visible light, *Appl. Catal., B*, 2016, **190**, 36–43, DOI: 10.1016/j.apcatb.2016.02.060.

9 U. Gupta and C. N. R. Rao, Hydrogen generation by water splitting using MoS_2 and other transition metal dichalcogenides, *Nano Energy*, 2017, **41**, 49–65, DOI: 10.1016/j.nanoen.2017.08.021.

10 R. Shen, L. Zhang, X. Chen, M. Jaroniec, N. Li and X. Li, Integrating 2D/2D CdS/α-Fe_2O_3 ultrathin bilayer Z-scheme heterojunction with metallic β-NiS nanosheet-based ohmic-junction for efficient photocatalytic H_2 evolution, *Appl. Catal., B*, 2020, **266**, 118619, DOI: 10.1016/j.apcatb.2020.118619.

11 J. Bai, R. Shen, Z. Jiang, P. Zhang, Y. Li and X. Li, Integration of 2D layered CdS/WO_3 S-scheme heterojunctions and metallic Ti_3C_2 MXene-based Ohmic junctions for effective photocatalytic H_2 generation, *Chin. J. Catal.*, 2022, **43**, 359–369, DOI: 10.1016/S1872-2067(21)63883-4.

12 Z. Liang, R. Shen, Y. H. Ng, P. Zhang, Q. Xiang and X. Li, A review on 2D MoS_2 cocatalysts in photocatalytic H_2 production, *J. Mater. Sci. Technol.*, 2020, **56**, 89–121, DOI: 10.1016/j.jmst.2020.04.032.

13 S. Cheng, Q. Xiong, C. Zhao and X. Yang, Synergism of 1D CdS/2D Modified $Ti_3C_2T_x$ MXene Heterojunctions for Boosted Photocatalytic Hydrogen Production, *Chin. J. Struct. Chem.*, 2022, **41**, 2208058–2208064, DOI: 10.14102/j.cnki.0254-5861.2022-0151.

14 S. Li, J. Sun and J. Guan, Strategies to improve electrocatalytic and photocatalytic performance of two-dimensional materials for hydrogen evolution reaction, *Chin. J. Catal.*, 2021, **42**, 511–556, DOI: 10.1016/S1872-2067(20)63693-2.

15 A. Fujishima and K. Honda, Electrochemical Photolysis of Water at a Semiconductor Electrode, *Nature*, 1972, **238**, 37–38, DOI: 10.1038/238037a0.

16 K. Maeda, Photocatalytic water splitting using semiconductor particles: history and recent developments, *J. Photochem. Photobiol., C*, 2011, **12**, 237–268, DOI: **10.1016/j.jphotochemrev.2011.07.001**.

17 R. Abe, Recent progress on photocatalytic and photoelectrochemical water splitting under visible light irradiation, *J. Photochem. Photobiol., C*, 2010, **11**, 179–209, DOI: **10.1016/j.jphotochemrev.2011.02.003**.

18 Z. Mei, G. Wang, S. Yan and J. Wang, Rapid Microwave-Assisted Synthesis of 2D/1D $ZnIn_2S_4/TiO_2$ S-scheme Heterojunction for Catalyzing Photocatalytic Hydrogen Evolution, *Acta Phys. Chim. Sin.*, 2020, 2009097, DOI: **10.3866/PKU.WHXB202009097**.

19 Z. Ding, H. Yu, X. Liu, N. He, X. Chen and H. Li, *et al.*, Prussian blue analogue derived cobalt–nickel phosphide/carbon nanotube composite as electrocatalyst for efficient and stable hydrogen evolution reaction in wide-pH environment, *J. Colloid Interface Sci.*, 2022, **616**, 210–220, DOI: **10.1016/j.jcis.2022.02.039**.

20 D. Liu, C. Li, J. Ge, C. Zhao, Q. Zhao and F. Zhang, *et al.*, 3D interconnected $g-C_3N_4$ hybridized with 2D Ti_3C_2 MXene nanosheets for enhancing visible light photocatalytic hydrogen evolution and dye contaminant elimination, *Appl. Surf. Sci.*, 2022, **579**, 152180, DOI: **10.1016/j.apsusc.2021.152180**.

21 D. Liu, C. Li, C. Zhao, Q. Zhao, T. Niu and L. Pan, *et al.*, Facile synthesis of three-dimensional hollow porous carbon doped polymeric carbon nitride with highly efficient photocatalytic performance, *Chem. Eng. J.*, 2022, **438**, 135623, DOI: **10.1016/j.cej.2022.135623**.

22 K. Pramoda and C. N. R. Rao, Two-Dimensional Materials and their Hetero-Superlattices for Photocatalytic Hydrogen Evolution Reaction, *ChemNanoMat*, 2022, **8**, e202200153, DOI: **10.1002/cnma.202200153**.

23 C. N. R. Rao, K. Pramoda, A. Saraswat, R. Singh, P. Vishnoi and N. Sagar, *et al.*, Superlattices of covalently cross-linked 2D materials for the hydrogen evolution reaction, *APL Mater.*, 2020, **8**, 020902, DOI: **10.1063/1.5135340**.

24 C. N. R. Rao, A. K. Sood, K. S. Subrahmanyam and A. Govindaraj, Graphene: The New Two-Dimensional Nanomaterial, *Angew. Chem., Int. Ed.*, 2009, **48**, 7752–7777, DOI: **10.1002/anie.200901678**.

25 F. Zhang, K. Yang, G. Liu, Y. Chen, M. Wang and S. Li, *et al.*, Recent advances on graphene: Synthesis, properties and applications, *Composites, Part A*, 2022, **160**, 107051, DOI: **10.1016/j.compositesa.2022.107051**.

26 L. Song, H. Li, Y. Zhang and J. Shi, Recent progress of two-dimensional metallic transition metal dichalcogenides: Syntheses, physical properties, and applications, *J. Appl. Phys.*, 2022, **131**, 060902, DOI: **10.1063/5.0083929**.

27 T. Li, T. Jing, D. Rao, S. Mourdikoudis, Y. Zuo and M. Wang, Two-dimensional materials for electrocatalysis and energy storage applications, *Inorg. Chem. Front.*, 2022, **9**, 6008–6046, DOI: **10.1039/D2QI01911F**.

28 A. Hannan, A. Khalil, N. Arshad, M. B. Tahir, A. G. Wattoo and M. K. Shahzad, Transition Metal Dichalcogenides for Photo/Electrochemical Energy-Based Applications, *Energy Technol.*, 2022, **10**, 2200546, DOI: **10.1002/ente.202200546**.

29 A. Mondal and A. Vomiero, 2D Transition Metal Dichalcogenides-Based Electrocatalysts for Hydrogen Evolution Reaction, *Adv. Funct. Mater.*, 2022, 2208994, DOI: **10.1002/adfm.202208994**.

30 Y. Xu, R. Ge, J. Yang, J. Li, S. Li and Y. Li, *et al.*, Molybdenum disulfide (MoS_2)-based electrocatalysts for hydrogen evolution reaction: From mechanism to manipulation, *J. Energy Chem.*, 2022, **74**, 45–71, DOI: **10.1016/j.jechem.2022.06.031**.

31 H. Li, L. Zhu, C. Li, Z. Wu, H. Li and Q. Chen, *et al.*, S-doping induced phase engineering of $MoSe_2$ for hydrogen evolution reaction, *Int. J. Hydrogen Energy*, 2022, **47**, 30371–30377, DOI: **10.1016/j.ijhydene.2022.07.008**.

32 G. F. Franklin, A. Balocchi, P.-L. Taberna, A. Barnabe, J. B. Barbosa and M. Blei, *et al.*, Mitigation of Edge and Surface States Effects in Two-Dimensional WS_2 for Photocatalytic H_2 Generation, *ChemSusChem*, 2022, **15**, e202200169, DOI: **10.1002/cssc.202200169**.

33 P. S. Tóth, G. Szabó, G. Bencsik, G. F. Samu, K. Rajeshwar and C. Janáky, Peeling off the surface: Pt-decoration of WSe_2 nanoflakes results in exceptional photoelectrochemical HER activity, *SusMat*, 2022, **2**, 749–760, DOI: **10.1002/sus2.86**.

34 P. V. Shinde, P. Mane, D. J. Late, B. Chakraborty and C. S. Rout, Promising 2D/2D $MoTe_2/Ti_3C_2T_x$ Hybrid Materials for Boosted Hydrogen Evolution Reaction, *ACS Appl. Energy Mater.*, 2021, **4**, 11886–11897, DOI: **10.1021/acsaem.1c02914**.

35 J. Radhakrishnan, S. Ratna and K. Biswas, Metal oxide/2D layered TMDs composites for H_2 evolution reaction via photocatalytic water splitting – A mini review, *Inorg. Chem. Commun.*, 2022, **145**, 109971, DOI: **10.1016/j.inoche.2022.109971**.

36 Y. Xiao, M. Zhou, J. Liu, J. Xu and L. Fu, Phase engineering of two-dimensional transition metal dichalcogenides, *Sci. China: Mater.*, 2019, **62**, 759–775, DOI: **10.1007/s40843-018-9398-1**.

37 J. Yao and G. Yang, 2D Layered Material Alloys: Synthesis and Application in Electronic and Optoelectronic Devices, *Adv. Sci.*, 2022, **9**, 2103036, DOI: **10.1002/advs.202103036**.

38 Z. Lin, B. R. Carvalho, E. Kahn, R. Lv, R. Rao and H. Terrones, *et al.*, Defect engineering of two-dimensional transition metal dichalcogenides, *2D Mater.*, 2016, **3**, 022002, DOI: **10.1088/2053-1583/3/2/022002**.

39 X.-G. Zhao, Z. Shi, X. Wang, H. Zou, Y. Fu and L. Zhang, Band structure engineering through van der Waals heterostructing superlattices of two-dimensional transition metal dichalcogenides, *InfoMat*, 2021, **3**, 201–211, DOI: **10.1002/inf2.12155**.

40 M. M. Ayyub, R. Singh and C. N. R. Rao, Hydrogen Generation by Solar Water Splitting Using 2D Nanomaterials, *Solar RRL*, 2020, **4**, 2000050, DOI: **10.1002/solr.202000050**.

41 B. Han and Y. H. Hu, MoS2 as a co-catalyst for photocatalytic hydrogen production from water, *Energy Sci. Eng.*, 2016, **4**, 285–304, DOI: **10.1002/ese3.128**.

42 D. Mouloua, A. Kotbi, G. Deokar, K. Kaja, M. El Marssi, E. L. Khakani and J. Mustapha, *et al.*, Recent Progress in the

Synthesis of MoS2 Thin Films for Sensing, Photovoltaic and Plasmonic Applications: A Review, *Materials*, 2021, **14**, 3283, DOI: **10.3390/ma14123283**.

43 C. N. R. Rao, U. Maitra and U. V. Waghmare, Extraordinary attributes of 2-dimensional MoS$_2$ nanosheets, *Chem. Phys. Lett.*, 2014, **609**, 172–183, DOI: **10.1016/j.cplett.2014.06.003**.

44 K. Pramoda, U. Gupta, I. Ahmad, R. Kumar and C. N. R. Rao, Assemblies of covalently cross-linked nanosheets of MoS$_2$ and of MoS$_2$–RGO: synthesis and novel properties, *J. Mater. Chem. A*, 2016, **4**, 8989–8994, DOI: **10.1039/C6TA00645K**.

45 S. Shi, Z. Sun and Y. H. Hu, Synthesis, stabilization and applications of 2-dimensional 1T metallic MoS$_2$, *J. Mater. Chem. A*, 2018, **6**, 23932–23977, DOI: **10.1039/C8TA08152B**.

46 J. Cao, Y. Zhang, C. Zhang, L. Cai, Z. Li and C. Zhou, Construction of defect-rich 1T-MoS$_2$ towards efficient electrocatalytic hydrogen evolution: recent advances and future perspectives, *Surf. Interfaces*, 2021, **25**, 101305, DOI: **10.1016/j.surfin.2021.101305**.

47 J. Cao, J. Zhou, Y. Zhang and X. Liu, A Clean and Facile Synthesis Strategy of MoS$_2$ Nanosheets Grown on Multi-Wall CNTs for Enhanced Hydrogen Evolution Reaction Performance, *Sci. Rep.*, 2017, **7**, 8825, DOI: **10.1038/s41598-017-09047-x**.

48 P. Wang, T. Jia and B. Wang, A critical review: 1D/2D nanostructured self-supported electrodes for electrochemical water splitting, *J. Power Sources*, 2020, **474**, 228621, DOI: **10.1016/j.jpowsour.2020.228621**.

49 S. Das, G. Swain and K. Parida, One step towards the 1T/2H-MoS$_2$ mixed phase: a journey from synthesis to application, *Mater. Chem. Front.*, 2021, **5**, 2143–2172, DOI: **10.1039/D0QM00802H**.

50 S. Pakhira and S. N. Upadhyay, Efficient electrocatalytic H2 evolution mediated by 2D Janus MoSSe transition metal dichalcogenide, *Sustainable Energy Fuels*, 2022, **6**, 1733–1752, DOI: **10.1039/D1SE02040D**.

51 D. C. Binwal, M. Kaur, K. Pramoda and C. N. R. Rao, HER activity of nanosheets of 2D solid solutions of MoSe$_2$ with MoS$_2$ and MoTe$_2$, *Bull. Mater. Sci.*, 2020, **43**, 313, DOI: **10.1007/s12034-020-02293-2**.

52 A. Mondal, A. Prabhakaran, S. Gupta and V. R. Subramanian, Boosting Photocatalytic Activity Using Reduced Graphene Oxide (RGO)/Semiconductor Nanocomposites: Issues and Future Scope, *ACS Omega*, 2021, **6**, 8734–8743, DOI: **10.1021/acsomega.0c06045**.

53 Y. Takaguchi, T. Tajima and H. Miyake, Hydrogen-Evolving CNT-Photocatalysts for Effective Use of Solar Energy, in *Nanocarbons for Energy Conversion: Supramolecular Approaches*, ed. N. Nakashima, Springer International Publishing, Cham, 2019, pp. 205–218, DOI: **10.1007/978-3-319-92917-0_9**.

54 S. Duraisamy, A. Ganguly, P. K. Sharma, J. Benson, J. Davis and P. Papakonstantinou, One-Step Hydrothermal Synthesis of Phase-Engineered MoS$_2$/MoO$_3$ Electrocatalysts for Hydrogen Evolution Reaction, *ACS Appl. Nano Mater.*, 2021, **4**, 2642–2656, DOI: **10.1021/acsanm.0c03274**.

55 J. Zhang, D. Han, Y. Wang, L. Wang, X. Chen and X. Qiao, *et al.*, Synergy between nanozymes and natural enzymes on the hybrid MoS$_2$ nanosheets/graphite microfiber for enhanced voltammetric determination of hydrogen peroxide, *Microchim. Acta*, 2020, **187**, 321, DOI: **10.1007/s00604-020-04299-3**.

56 M. Wu, J. Zhan, K. Wu, Z. Li, L. Wang and B. Geng, *et al.*, Metallic 1T MoS$_2$ nanosheet arrays vertically grown on activated carbon fiber cloth for enhanced Li-ion storage performance, *J. Mater. Chem. A*, 2017, **5**, 14061–14069, DOI: **10.1039/C7TA03497K**.

57 P. Tiwari, D. Janas and R. Chandra, Self-standing MoS$_2$/CNT and MnO$_2$/CNT one dimensional core shell heterostructures for asymmetric supercapacitor application, *Carbon*, 2021, **177**, 291–303, DOI: **10.1016/j.carbon.2021.02.080**.

58 X. Zang, Y. Qin, T. Wang, F. Li, Q. Shao and N. Cao, 1T/2H Mixed Phase MoS$_2$ Nanosheets Integrated by a 3D Nitrogen-Doped Graphene Derivative for Enhanced Electrocatalytic Hydrogen Evolution, *ACS Appl. Mater. Interfaces*, 2020, **12**, 55884–55893, DOI: **10.1021/acsami.0c16537**.

59 U. Gupta, B. S. Naidu, U. Maitra, A. Singh, S. N. Shirodkar and U. V. Waghmare, *et al.*, Characterization of few-layer 1T-MoSe$_2$ and its superior performance in the visible-light induced hydrogen evolution reaction, *APL Mater.*, 2014, **2**, 092802, DOI: **10.1063/1.4892976**.

60 R. N. Jenjeti, R. Kumar, A. Sellam and S. Sampath, High Stability of 1T-Phase MoS$_{2x}$Se$_{2(1-x)}$ Monolayers Under Ambient Conditions, *J. Phys. Chem. C*, 2021, **125**, 8407–8417, DOI: **10.1021/acs.jpcc.1c00212**.

61 K. Namsheer, S. R. Polaki and C. S. Rout, Molybdenum sulfo-selenides grown on surface engineered vertically aligned graphitic petal arrays for solid-state supercapacitors, *J. Energy Storage*, 2022, **52**, 105007, DOI: **10.1016/j.est.2022.105007**.

62 H. Fan, R. Wu, H. Liu, X. Yang, Y. Sun and C. Chen, Synthesis of metal-phase-assisted 1T@2H-MoS$_2$ nanosheet-coated black TiO$_2$ spheres with visible light photocatalytic activities, *J. Mater. Sci.*, 2018, 53, DOI: **10.1007/s10853-018-2266-8**.

63 H. Niu, Z. Zou, Q. Wang, K. Zhu, K. Ye and G. Wang, *et al.*, Structurally stable ultrathin 1T-2H MoS$_2$ heterostructures coaxially aligned on carbon nanofibers toward superhigh-energy-density supercapacitor and enhanced electrocatalysis, *Chem. Eng. J.*, 2020, **399**, 125672, DOI: **10.1016/j.cej.2020.125672**.

64 N. Kuniyil, S. R. Koottumvathukkal Anil Raj and C. S. Rout, Selective Growth of Molybdenum Sulfo-Selenides on a Defect-Rich Carbon Nanotube Skeleton for Efficient Energy Storage and Hydrogen Generation Applications, *Energy Fuels*, 2022, **36**, 13346–13355, DOI: **10.1021/acs.energyfuels.2c02799**.

65 N. Li, Y. Zhang, M. Jia, X. Lv, X. Li and R. Li, *et al.*, 1T/2H MoSe$_2$-on-MXene heterostructure as bifunctional electrocatalyst for efficient overall water splitting, *Electrochim. Acta*, 2019, **326**, 134976, DOI: **10.1016/j.electacta.2019.134976**.

66 F. T. Johra and W.-G. Jung, Hydrothermally reduced graphene oxide as a supercapacitor, *Appl. Surf. Sci.*, 2015, **357**, 1911–1914, DOI: **10.1016/j.apsusc.2015.09.128**.

67 S. D. Gardner, C. S. K. Singamsetty, G. L. Booth, G.-R. He and C. U. Pittman, Surface characterization of carbon fibers

using angle-resolved XPS and ISS, *Carbon*, 1995, **33**, 587–595, DOI: 10.1016/0008-6223(94)00144-O.

68 D. C. Binwal, K. Pramoda, A. Zak, M. Kaur, P. Chithaiah and C. N. R. Rao, Nanocomposites of 1D MoS$_2$ with Polymer-Functionalized Nanotubes of Carbon and Borocarbonitride, and Their HER Activity, *ACS Appl. Energy Mater.*, 2021, **4**, 2339–2347, DOI: 10.1021/acsaem.0c02874.

69 P. Vishnoi, K. Pramoda, U. Gupta, M. Chhetri, R. G. Balakrishna and C. N. R. Rao, Covalently Linked Heterostructures of Phosphorene with MoS$_2$/MoSe$_2$ and Their Remarkable Hydrogen Evolution Reaction Activity, *ACS Appl. Mater. Interfaces*, 2019, **11**, 27780–27787, DOI: 10.1021/acsami.9b06910.

70 K. Pramoda, S. Servottam, M. Kaur and C. N. R. Rao, Layered Nanocomposites of Polymer-Functionalized Reduced Graphene Oxide and Borocarbonitride with MoS$_2$ and MoSe$_2$ and Their Hydrogen Evolution Reaction Activity, *ACS Appl. Nano Mater.*, 2020, **3**, 1792–1799, DOI: 10.1021/acsanm.9b02482.